View metadata, citation and similar papers at core.ac.uk

brought to you by CORE

provided by Archivio istituzionale della ricerca - Università di Modena e Reggio Emilia

Applied Clay Science xxx (xxxx) xxx-xxx

Contents lists available at ScienceDirect

Applied Clay Science

journal homepage: http://ees.elsevier.com

Research paper

A new material based on montmorillonite and Cu(II)-phenanthroline complex for effective capture of ammonia from gas phase

Elena Castellini [a,*], Daniele Malferrari [a], Fabrizio Bernini [a], Beatrice Bighi [a], Adele Mucci [a], Ignacio Claro Sainz-Díaz [b], Aida Serrano [c,d], German R. Castro [c,e], Maria Franca Brigatti [a], Marco Borsari [a]

[a] Department of Chemical and Geological Sciences, University of Modena and Reggio Emilia, Via Campi 103, Modena I-41125, Italy
[b] Instituto Andaluz de Ciencias de la Tierra (CSIC-UGR), Av. de las Palmeras, 4, 18100-Armilla, Granada, Spain
[c] SpLine, Spanish CRG BM25 Beamline at The European Synchrotron (The ESRF), 71 Avenue des Martyrs, Grenoble F-38000, France
[d] Instituto de Cerámica y Vidrio (ICV), CSIC, Kelsen 5, Madrid E-28049, Spain
[e] Instituto de Ciencia de Materiales de Madrid (ICMM), CSIC, Sor Juana Inés de la Cruz 3, Madrid E-28049, Spain

ARTICLE INFO

Keywords
Gas trapping
Montmorillonite
Intercalation
Copper complexes
Interlayer

ABSTRACT

The intercalation of $[Cu(Phen)(H_2O)_2]^{2+}$ (CuPhen) in montmorillonite (Mt) produces a stable hybrid material that is very efficient in removing NH_3 from gas phase even at extremely low pressures.The process was studied by elemental analysis, X-ray powder diffraction, thermal analysis coupled with evolved gas mass spectrometry and DR UV–Vis, NMR and X-ray absorption spectroscopy. The adsorption of CuPhen on Mt consists of two consecutive steps. During the first one, CuPhen intercalates alone into Mt through a cation exchange process, afterwards CuPhen and SO_4^{2-} ions entry jointly into the mineral interlayer. The two-steps adsorption process is described by a VI-type isotherm, successfully fitted by two independent Frumkin isotherms. NH_3 trapping is long-lasting, easy, fast even at extremely low gas pressure and reversible under mild conditions. Mt containing CuPhen always results well performant in removing ammonia from gas phase, but an appreciably higher adsorption capacity of NH_3 is obtained when SO_4^{2-} ion is absent from the interlayer. This hybrid montmorillonite is thus a promising material to be used in industrial or environmental contexts, as an efficient air-cleaner.

1. Introduction

The intercalation of organic species into the interlayer of 2:1 layer silicates, such as montmorillonite, is well documented in literature (Brigatti et al., 2011). The derived hybrid materials are of great importance not only under the perspective of fundamental investigation, but also for their applications in different fields, from biomedicine and pharmacy to energy storage and environmental protection (Bergaya and Lagaly, 2011). One example of these materials, where the functionalization of the interlayer leads to intriguing properties, is montmorillonite intercalated with a μ-oxo Fe^{3+}-phenanthroline complex (Mt-Fe^{3+}Phen) (Bernini et al., 2015; Brigatti et al., 2017; Sainz-Díaz et al., 2018). This hybrid material was proved to efficiently trap sulfur-bearing gas phases such as thiols and H_2S, even at extremely low concentration, with a relevant environmental benefit. In both the cases, the immobilization mechanism occurs through a multistep process involving first a redox reaction and then the covalent binding of the R-SH or H_2S molecule (Bernini et al., 2017; Malferrari et al., 2018). In addition, Mt-Fe^{3+}Phen was recently used also to successfully entrap gaseous naphthalene and chloro-naphthalene (Castellini et al., 2019a).

In the context of capture of toxic gases, however, intercalated montmorillonite is in general poorly effective for the entrapment of ammonia, which, even at low concentration levels, is a potentially hazardous chemical, notoriously harmful to both industrial processes and human beings. Ammonia is an extremely diffused gas, emitted by both biogenic and anthropogenic sources (Barin et al., 2017) and thus the establishment of effective protection mechanisms on ammonia exposure

Abbreviations: Mt, montmorillonite STx-1b from Gonzales County (Texas, USA) obtained from the Clay Minerals Society (The Clay Minerals Society, Source Clays Repository, University of Missouri, Columbia, MO); CuPhen, $[Cu[(Phen)(H_2O)_2]^{2+}$; Mt-CuPhen, solid hybrid material obtained by Mt treated with CuPhen complex; Mt-$CuPhen_{sat}$, Mt saturated with CuPhen, *i.e.*, solid hybrid material obtained by the treatment of Mt with a 6 mM solution of CuPhen complex; Mt-$CuPhen_{semisat}$, Mt semi-saturated with CuPhen, *i.e.*, solid hybrid material obtained by the treatment of Mt with a 2.5 mM solution of CuPhen complex; Mt-$CuPhen_{sat}$-NH_3, Mt-$CuPhen_{sat}$ exposed to NH_3vapors; Mt-$CuPhen_{semisat}$-NH_3, Mt-$CuPhen_{semisat}$ exposed to NH_3vapors..

* Corresponding author at: Department of Chemical and Geological Sciences, University of Modena and Reggio Emilia, Via Campi 103, Modena I-41125, Italy.
E-mail address: elena.castellini@unimore.it (E. Castellini)

https://doi.org/10.1016/j.clay.2019.105386
Received 28 August 2019; Received in revised form 8 November 2019; Accepted 21 November 2019
Available online xxx
0169-1317/© 2018.

UNCORRECTED PROOF

is an extremely relevant topic. Depending on the application, a variety of techniques for the elimination of gaseous ammonia exists, such as adsorption, condensation, biofiltration, catalytic combustion, catalytic decomposition, thermal and selective catalytic oxidation (Wójtowicz et al., 2000; Chung et al., 2001; Chen et al., 2016). Selective catalytic oxidation of ammonia into nitrogen and water vapor is among the preferred technologies for the treatment of large gas flows containing oxygen and low concentrations of ammonia (Busca and Pistarino, 2003; Jabłonska and Palkovits, 2016). This technology, which commonly exploits copper-based catalysts such as polycrystalline copper (Mayera et al., 2011), Cu-oxides (He et al., 2007), Cu-spinels (Yue et al., 2014), Cu-exchanged zeolites (Lenihan and Curtin, 2009), and Cu-modified (pillared) layer silicates (Liu et al., 2016), is efficient, but works at temperatures higher than 400 °C.

The aim of this work is to prepare and characterize the properties of a new hybrid material obtained by montmorillonite intercalated with the copper-phenanthroline complex $[Cu(Phen)(H_2O)_2]^{2+}$ (CuPhen) and apply it in removing gaseous ammonia, exploring also extremely low pressures. Factors affecting the adsorption of NH_3, like initial pressure, adsorbent composition and contact time, were analyzed. Besides, given the main role played by CuPhen in NH_3 uptake, the adsorption process of this complex on montmorillonite was investigated in detail. To allow the reuse of the adsorbent, the conditions for its regeneration were determined as well.

2. Experimental section

2.1. Materials

Montmorillonite STx-1b (Mt) from Gonzales County (Texas, USA) was obtained from the Clay Minerals Society, chemical formula: $^{[4]}(Si_{7.753}\ Al_{0.247})\ ^{[6]}(Al_{3.281}\ Mg_{0.558}\ Fe_{0.136}\ Ti_{0.024}\ Mn_{0.002})\ ^{[12]}(Ca_{0.341}\ Na_{0.039}\ K_{0.061})\ O_{20}\ (OH)_4$, cation exchange capacity (CEC): 66.1 (±2.1) meq/100 g (Castellini et al., 2017). 1,10-phenanthroline monohydrate (Phen) and anhydrous NH_3 (>99 analytical grade purity) were purchased from Sigma Aldrich, $CuSO_4 \bullet 5H_2O$ (>99% analytical grade purity) from Carlo Erba.

2.2. Experimental procedure

2.2.1. Adsorption isotherms of CuPhen on Mt

2 mL of CuPhen solution with starting concentrations ranging from 0.2 to 8 mM was added to 16 mg of Mt. The starting concentration of each CuPhen solution was determined spectrophotometrically. Each dispersion was shaken for 1 h at 250 rpm in an orbital incubator at $T = 20$ °C (Stuard Scientific Orbital Incubator SI50) to ensure to obtain equilibrium conditions. Then, the separated supernatant was further centrifuged at 14000 rpm for 1 min. The number of CuPhen adsorbed moles was determined by the decrease in the UV–Vis spectra of the CuPhen solutions and checked by elemental analysis performed on solids (C, N, S content). The adsorption experiments were repeated 5 times in the same conditions to obtain mean values with a statistical significance.

The isotherm consists of two steps whose parameters were calculated by data fitting with Origin Pro 8.0 software. The maximum adsorption of the first step c is equal to CEC (semi-saturation), the second step is twice the first one (saturation).

2.2.2. Preparation of montmorillonite saturated (Mt-CuPhen$_{sat}$) and semi-saturated (Mt-CuPhen$_{semisat}$) with CuPhen complex

Solid $CuSO_4 \bullet 5H_2O$ was slowly dissolved at room temperature in two well-stirred Phen solution in order to obtain CuPhen solutions of concentrations 2.5 and 6 mM. Adsorption measurements showed that starting CuPhen concentrations of 2.5 and 6 mM give Mt semi-saturation and saturation, respectively. 80 mg of Mt were dispersed in 10 mL of each solutions and shaken for 1 h at 250 rpm at room temperature (Stuard Scientific Orbital Incubator SI50). Solid-liquid separation was achieved *via* centrifugation at 14000 for 1 min (Thermo mod. Espresso). The separated solids were washed several times with distilled water and dried at 30 °C to obtain semi-saturated (Mt-CuPhen$_{semisat}$) and saturated (Mt-CuPhen$_{sat}$) hybrid material .

2.2.3. Exposure of Mt-CuPhen$_{sat}$ and Mt-CuPhen$_{semisat}$ to gaseous NH_3

A micro-scale apparatus was developed to measure the ammonia adsorption capacity of Mt-CuPhen$_{semisat}$ and Mt-CuPhen$_{sat}$ up to 250 h. Approximately 50 mg of both samples were placed in a glass Petri dish into a closed glass box. The glass box hosts an inner and outer gas hose and ammonia gas was injected to yield a constant partial pressure of 250 Pa. Vapor composition was accurately tuned by means of calibrated mass flow controllers (Alltech Digital Flow Check-HR) and gas mixing valves. The content in C, N and S of the exposed samples (Mt-CuPhen$_{semisat}$-NH_3 and Mt-CuPhen$_{sat}$-NH_3) as a function of time was determined by elemental analysis. The data are the mean values of 5 repeated experiments.

2.2.4. Exposure of Mt-CuPhen$_{semisat}$ to gaseous NH_3 at extremely low pressures

Experiments were performed to study the ability of Mt-CuPhen$_{semisat}$ to efficiently remove NH_3 also at extremely low starting pressure (P^0_{NH3}) values, specifically at 5.7 and 11.9 Pa, in a closed system. The experiments were carried out in closed boxes at different times (time range: 0.1–24 h), therefore in the condition of progressive decrease of the NH_3 pressure. For each time point, 5 mg of Mt-CuPhen$_{semisat}$ dispersed in a Petri glass and a small beaker containing a proper volume of a NH_4OH solution were placed in a closed glass box (volume = 0.31 L). Inside the closed boxes 5 μL of a 0.1397 M NH_4OH solution or 10 μL of a 0.1468 M NH_4OH solution were put in a beaker and vaporized in order to obtain, at $T = 30$ °C, the P^0_{NH3} values of 5.7 and 11.9 Pa, respectively. The C, N, S contents of the samples exposed for different times were determined using elemental analysis, thus providing info on the adsorption kinetics of NH_3 at very low-pressure values. Also these kinetic experiments were repeated 5 times.

2.2.5. Regeneration of the exposed materials

Regeneration of exposed materials was performed heating Mt-CuPhen$_{semisat}$-NH_3 and Mt-CuPhen$_{sat}$-NH_3 in an oven at 110 °C for 5 min. Subsequent NH_3 adsorption was made as described in paragraph 2.2.3. Up to ten adsorption-regeneration cycles were performed.

2.3. Techniques employed to characterize the hybrid material before and after exposure to NH_3

The elemental analyses (C, N, S) were determined by using a Carlo Erba Elemental Analyser (Model 1106), each measurement was repeated five times. UV–Vis and diffuse-reflectance (DR)UV–Vis measurements (V-570 Jasco instrument) were achieved on solutions and solid samples, respectively. In solution measurements were made in the λ range 190–800 nm with a resolution of 1 nm. DR-UV–Vis measurements on powder samples were recorded in the λ range 220–2000 nm using an integrating sphere (Jasco model ISN-470), $BaSO_4$ was used as the reference.

X-ray powder diffraction (XRPD) patterns were obtained by a Philips X'Pert PRO diffractometer equipped with first generation Real Time Multiple Strip (RTMS) detector. Experimental conditions were: incident beam, Cu *K*α radiation (1.54056 Å) at 40 kV and 40 mA; filter, nickel; Soller slits, 0.04 rad; anti-scatter mask, 20 mm; anti-scatter slit, 1/4°; divergence slit, 1/4°. Diffracted beam: anti-scatter mask, 5.0 mm; Soller slits, 0.04 rad; integration time, 120 s in continuous scanning (length of 2.12 °2θ corresponding to a step size of 0.0170 °2θ per s).

UNCORRECTED PROOF

Measurements were collected in the 3–70 °2θ range. The d_{001} variations were measured from (00*l*) oriented mounts; each d_{001} value was determined at the mid-height of the reflection through X-Pert High Score Plus software.

A simultaneous, thermo-gravimetric (TGA) and thermo-differential (DTA) analyser (Seiko SSC 5200, with a Pt crucible and Pt/Pt–Rh thermocouples) was used to characterize the thermal properties of the materials. The thermo-analyser is equipped with a quadrupole mass spectrometer (ESS, GeneSysQuadstar 422) able to detect the gases evolved during thermal reactions (MSEGA). Experimental conditions were: heating rate: 20.0 °C/min; heating range: 25–1000 °C; data measurement: every 0.5 s; purging gas: ultrapure helium, flow rate: 100 μL/min.

The volatile products evolved during heating were detected by mass spectrometer in Multiple Ion Detection mode (MID) which allows the qualitative determination of evolved gasses *vs.* temperature or time checking the intensity of the signals related to the *m/z* ratios 18 for H_2O, 15 for NH_3, 30 for NO and NO_2, 44 for CO_2, 46 for NO_2, and 64 for SO_2 (m/z is the dimensionless ratio between the mass number and the charge of an ion); SEM detector of the spectrometer operated at 900 V with 1 s of integration time on each measured m/z signal.

^{1}H magic angle spinning (MAS) NMR spectra on Mt-CuPhen$_{sat}$ and Mt-CuPhen$_{sat}$-NH_3 were acquired at 300 K using a an AVANCE III HD 600 Bruker spectrometer equipped with a 2.5 mm H/X CPMAS probe operating at 600.13 MHz for ^{1}H. Zirconia rotors of 2.5 mm o.d. were used and spun at a MAS rate of 30 and 33 kHz rate, using DEPTH sequence in order to remove baseline distortions (Giustetto et al., 2011). The parameters used were: 125 kHz spectral width, 10 s relaxation delay, 2.4 μs 90° pulse, 4 k data points and 32 or 64 scans. The empty rotor ^{1}H spectrum was subtracted to compensate for background effects. All chemical shifts were referenced by adjusting the spectrometer field to the value corresponding to 38.48 ppm chemical shift for the deshielded line of the adamantane ^{13}C NMR signal, as previously reported (Castellini et al., 2017).

X-ray absorption spectroscopy (XAS) measurements were performed at the Cu *K*-edge (8979 eV) at the Spanish CRG beamline BM25 at The European Synchrotron (ESRF), Grenoble (France). The beamline monochromator is a pseudo channel-cut type with two Si(111) crystals refrigerated at 200 K by a homemade ethanol cooling system. XAS spectra were collected in transmission mode at room temperature on pellets prepared by mixing uniformly the powered samples and cellulose. The transmission signal was recorded with an ionization chamber refilled with 50% N_2 and 50% Ar. The energy of XAS data was calibrated with a metallic Cu foil. Reference powder materials Cu_2O, CuO, CuS, $CuSO_4 \bullet 5H_2O$ and $Cu_3(CO_3)_2(OH)_2$ were used for the analysis. The XAS spectra were recorded over a wide energy range across the Cu *K*-absorption edge with 0.25 eV energy step in the X-ray absorption near-edge structure (XANES) region. The X-ray absorption data were analyzed with a standard procedure using Demeter package (Ravel and Newville, 2005).

3. Results and discussion

3.1. Adsorption of CuPhen onto montmorillonite

Adsorption behavior of CuPhen complex onto Mt is described in Fig. 1, which reports the moles of adsorbed CuPhen per mass unit of montmorillonite (q), as a function of CuPhen concentration in solution at equilibrium, [CuPhen]. Function q progressively increases with increasing [CuPhen], to reach a limit value at about 0.65 moles/Kg Mt. Furthermore, as already observed for the adsorption of the μ-oxo dinuclear iron-phenanthroline complex onto Mt (Bernini et al., 2015), an inflection point close to half of the q limit value clearly outlines the presence of two steps in the adsorption process (Fig. 1a). This adsorption behavior identifies a VI type isotherm (Gregg and Sing, 1982;

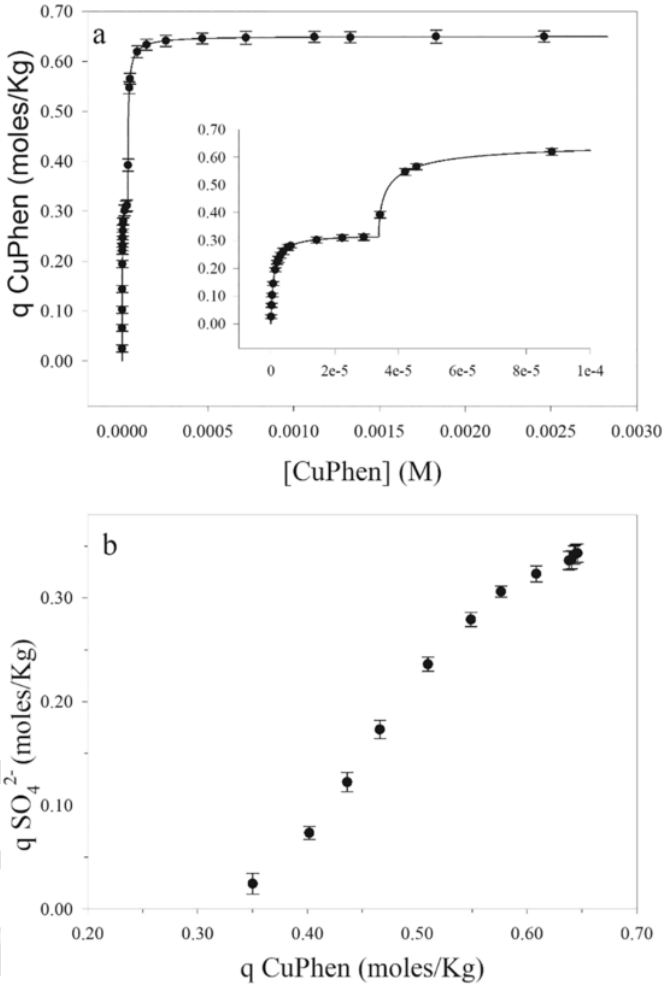

Fig. 1. a) Plot of the moles of CuPhen adsorbed per mass unit of Mt, q, as a function of the CuPhen equilibrium concentration, T = 25 °C. Curves were obtained by the best fitting of the data calculated using two independent Frumkin isotherms. b) SO_4^{2-} adsorbed moles per mass unit of Mt as a function of the number of CuPhen adsorbed moles per mass unit of Mt. The reported data are the mean values of 5 repeated experiments.

Sing et al., 1966; Bernini et al., 2015). The inflection point occurs at a q value corresponding to the CEC of Mt ($q_{inflection}$ about 0.31 moles/Kg; CEC = 0.661 eq/Kg = 0.330 moles/Kg). Elemental analysis revealed that in the second adsorption step sulphate ions are co-adsorbed with the complex in an amount matching the charge excess of adsorbed complex with respect to CEC of Mt (about 0.343 moles/Mt Kg in Mt-CuPhen$_{sat}$). In Fig. 1b the number of adsorbed moles of SO_4^{2-}/Mt Kg *vs.* q is reported.

Every step can be well described by the Frumkin adsorption model (Fig. 2a), thus the overall curve (Fig. 1a) was fitted by two independent Frumkin isotherms using the following equation (Bernini et al., 2015):

$$q = K_{ads,I}\, q_{max,I}\, c / \left[\exp\left(2a_I\, q/q_{max,I}\right) + K_{ads,I}\, c\right] + K_{ads,II}\, q_{max,II}\, (c - c_0) / \left[\exp\left(2a_{II}\, q/q_{max,II}\right) + K_{ads,II}\, (c - c_0)\right] \quad (1)$$

where: I = first adsorption step; II = second adsorption step; K_{ads} = adsorption constant; c = adsorbate equilibrium concentration expressed as moles × dm^{-3}; q = number of adsorbed CuPhen moles for Mt mass unit, expressed as moles × Kg^{-1}; q_{max} = upper limit value of q; a = Frumkin interaction parameter; c_0 = adsorbate critical concentration corresponding to the starting point of step II (Fig. 1a). The sec-

UNCORRECTED

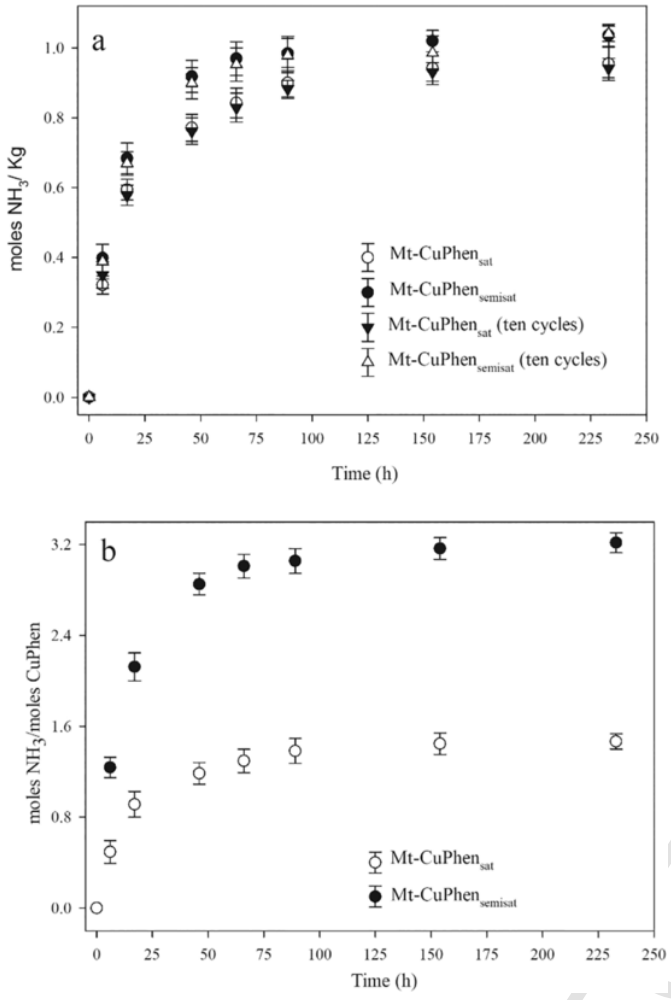

Fig. 2. (a) Plot of the NH_3 moles adsorbed per mass unit of Mt by Mt-CuPhen$_{sat}$ and Mt-CuPhen$_{semisat}$ pristine materials and after ten regeneration cycles; (b) NH_3/CuPhen molar ratio in Mt-CuPhen$_{semisat}$ and Mt-CuPhen$_{sat}$ as a function of the time of exposure to NH_3. P_{NH3} = 250 Pa. The reported data are the mean values of 5 repeated experiments.

ond step starts only at the end of the first one. The correlation coefficient of the model described by eq. (1) results to be $r^2 = 0.997$.

The first step of the adsorption process involves only a cation exchange between the positively charged complex and the exchangeable cations of Mt, whereas the second one occurs with the formation of a structure in the interlayer containing both SO_4^{2-} and CuPhen (Fig. 1b). The value of $q_{max,I}$ of first adsorption step corresponds to the Mt CEC value ($q_{max,I}$ = 0.322 ± 0.007 moles/Kg; Mt CEC = 0.330 moles/Kg), whereas also the $q_{max,II}$ value ($q_{max,II}$ = 0.329 ± 0.007 moles/Kg) is very similar to CEC (Table 1). SO_4^{2-} adsorption starts after achievement of $q_{max,I} \cong CEC_{Mt}$ and gradually increases with q up to a limit value (Fig. 1b) corresponding to a molar ratio CuPhen/SO_4^{2-} = 2 ($q_{max}SO_4^{2-}$ = 0.343 moles/Kg).

Table 1
Parameters of the Frumkin model obtained by fitting the q *vs.* [CuPhen] data with two independent Frumkin isotherms (Eq. (1)) using Origin Pro 8.0 software.

$q_{max,\,I}$ (moles/Kg)	0.322 ± 0.007
$q_{max,\,II}$ (moles/Kg)	0.329 ± 0.007
$K_{ads,\,I}$ (L/mol)	1.21 ± 0.31 10^6
$K_{ads,\,II}$ (L/mol)	8.87 ± 0.41 10^5
a_I	0.06 ± 0.01
a_{II}	0.89 ± 0.01

The obtained a_I and a_{II} values (a_I = 0.06 ± 0.01; a_{II} = 0.89 ± 0.01) indicate repulsive interactions among the adsorbed molecules, being $a_{II} > a_I$, as expected due to the increase of the electrostatic repulsions following to stepwise filling of the interlayer. The a_I and a_{II} values are lower if compared to the corresponding obtained for iron-phenanthroline complex (a_I = 0.10 and a_{II} = 1.89, Bernini et al., 2015), in line with the lower charge and dimension of the Cu^{2+} complex.

Obtained K_{ads} values indicate very high stability for adsorbed species. As found for the μ-oxo di-nuclear iron-phenanthroline complex (Bernini et al., 2015), the K_{ads} for the first step (K_{ads} = 1.21 ± 0.31 10^6 L/mol) is higher than that of the second one (K_{ads} = 8.87 ± 0.41 10^5 L/mol).

3.2. NH_3 capture by Mt-CuPhen$_{semisat}$ and Mt-CuPhen$_{sat}$

The interaction of NH_3 with Mt-CuPhen$_{semisat}$ and Mt-CuPhen$_{sat}$ was quantitatively characterized by measuring the N content as a function of time. For both samples, the NH_3 adsorption process can be considered completed after 150 h when P_{NH3} = 250 Pa (Fig. 2). Afterward the N content remains constant up to 230 h. The total amount of NH_3 adsorbed is greater for Mt-CuPhen$_{semisat}$ than for Mt-CuPhen$_{sat}$ (1.05 moles of NH_3 per 1Kg of Mt-CuPhen$_{semisat}$ instead of 0.96 moles of NH_3 per 1Kg of Mt-CuPhen$_{sat}$). The NH_3/CuPhen molar ratio is approximately 3.0 for Mt-CuPhen$_{semisat}$, while that corresponding for CuPhen$_{sat}$ is roughly 1.5 (Fig. 2).

3.3. Capture of gaseous NH_3 at extremely low pressure

Fig. 3 shows the micromoles of gaseous NH_3 removed by 5 mg of Mt-CuPhen$_{semisat}$ as a function of time at extremely low starting pressure values of NH_3 (P^0_{NH3} = 5.7 and 11.9 Pa) at 30 °C. The starting micromoles of gaseous NH_3 at P^0_{NH3} = 5.7 and 11.9 Pa in the glass box before the entrapping are represented by the horizontal lines. In both cases, the capture is fast and the decrease of gaseous NH_3 is high: at P^0_{NH3} = 5.7 Pa, the amount of removed NH_3 is 75.2%, while at P^0_{NH3} = 11.9 Pa, it is 89.0%. It is worth noting that the residual NH_3 pressure after the entrapping accomplishment is nearly the same in the two cases: being 1.45 Pa and 1.31 Pa for P^0_{NH3} 5.7 and 11.9 Pa, respectively. This fact suggests that for pressure lower than about 1.3 Pa Mt-CuPhen$_{semisat}$ material is inactive or its entrapping rate very slow.

3.4. DR UV–Vis and FT-IR measurements

DR UV–Vis spectra of Mt-CuPhen$_{sat}$ and CuPhen$_{semisat}$ are qualitatively very similar and present main bands related both to Mt and to CuPhen complex (Fig. 4): i) a band at 270 nm and an evident shoulder at 300 nm related to Phen ligand transitions (see also the UV–Vis spectrum of CuPhen crystals in S1); ii) a very large band with maximum at about 780 (Mt-CuPhen$_{sat}$) and 710 nm (Mt-CuPhen$_{semisat}$), related to Cu(II) d → d transition, partially overlapped to a band at 920 nm, probably due to an overtone of H_2O molecules coordinating the Cu^{2+}. When exposed to NH_3, the signals at 780 and 710 nm shift toward lower wavelengths (maximum at λ = 630 nm for Mt-CuPhen$_{semisat}$ and λ = 670 nm for Mt-CuPhen$_{sat}$, respectively) and the intensity of the signal at 920 nm strongly decreases, suggesting that the capture of NH_3 involves both the Cu^{2+} coordination and the binding H_2O molecules.

DR UV–Vis spectrum of CuPhen crystals is reported in S1 (Fig. S1); the band of the spectrum related to Cu(II) d → d transition shows the maximum at 686 nm, according to a distorted octahedral geometry.

The FT-IR spectra of Mt-CuPhen$_{sat}$ before and after exposure to NH_3 are reported in S2 (Fig. S2), no significant differences are observed between them.

UNCORRECTED PROOF

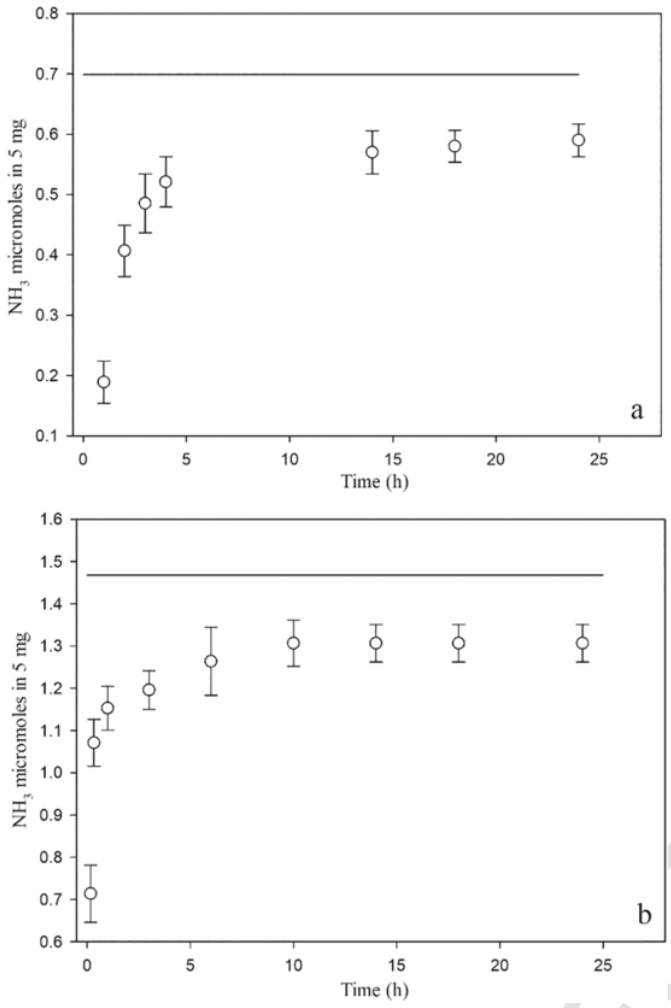

Fig. 3. Micromoles of NH_3 immobilized by 5 mg of Mt-CuPhen$_{semisat}$ in closed systems at P^0_{NH3} = 5.7 Pa (a) and 11.9 Pa (b) as a function of time. T = 30 °C. The horizontal line represents the starting micromoles of NH_3 present in the glass box before the capture takes place. The reported data are the mean values of 5 repeated experiments.

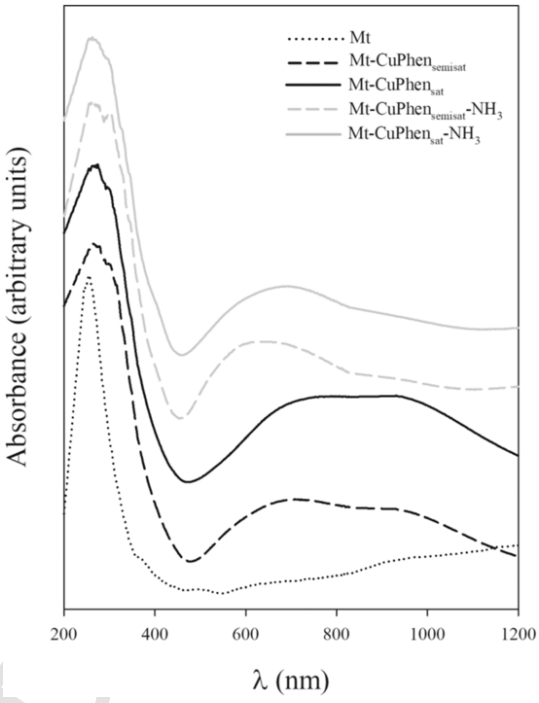

Fig. 4. DR UV–Vis spectra of Mt, Mt-CuPhen$_{sat}$ and Mt-CuPhen$_{semisat}$ before and after exposure to NH_3. Curves are shifted on y axis for sake of clarity.

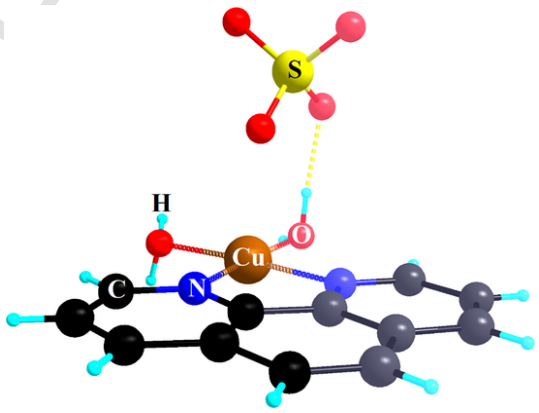

Fig. 5. View of the molecular structure of the synthesized CuPhen complex. Dashed yellow line indicates hydrogen-bonding between coordinated water and SO_4^{2-} group. (For interpretation of the references to colour in this figure legend, the reader is referred to the web version of this article.)

3.5. XRD analysis

The synthesized CuPhen crystal (see S3, Fig. S3, Table S3a and Table S3b) belongs to C2/c monoclinic space group (unit cell parameters: a = 1.4875(1), b = 1.3834(1), c = 0.70161(5) nm, β = 108.644(2)°) and presents a structural arrangement very similar to that obtained by Hu et al., 2009. Cu atom is linked to two nitrogen (Cu-N = 2.005(1) Å) and two oxygen atoms (Cu-O = 1.9715(9)Å) of the H_2O molecules to form a square planar coordination. Oxygen atom from SO_4^{2-} group is not directly coordinated to Cu ions. However, crystal packing of the complex implies that two oxygen atoms from SO_4^{2-} anions, occurring at a distance of 2.466(1) Å from Cu, identify an expanded octahedral coordination. The tetrahedral SO_4^{2-} groups form hydrogen-bonding interactions with the coordinated water ligands where H_2O acts as donors and SO_4^{2-} groups as acceptors (Fig. 5).

Fig. 6 shows the powder X-ray diffraction patterns ($3.5 \leq 2\theta^\circ \leq 8.5$) of untreated Mt, Mt-CuPhen$_{semisat}$ and Mt-CuPhen$_{sat}$ before and after NH_3 exposure. The variation of 001 reflection position is mostly related to the type of occupying molecules in the interlayer space (*e.g.*, water, cations, organometallic complexes), whereas the broadening of 001 reflection can be attributed to the layer stacking disorder.

For the untreated montmorillonite the 001 reflection shows a d-value of 1.51 nm, consistent with an interlayer occupancy of hydrated Ca cations (Castellini et al., 2017). This value can be interpreted as the sum of basal spacing corresponding to 2:1 layer, which is approximately 1 nm, plus 0.5 nm, which corresponds to di-hydrated Ca^{2+} cation. After the treatment with 2.5 mM CuPhen solution, 001 reflection of sample CuPhen$_{semisat}$ changes both in d-value and shape, namely: i) 001 reflection displaces toward lower d-value (1.32 nm), consistently with reduced interlayer space size following from substitution in interlayer of CuPhen species without sulphate anions (approximately 0.32 nm thick) for di-hydrated Ca^{2+}; ii) measured d_{001}-value is consistent with a square planar configuration of CuPhen in which Cu^{2+} coordinates nitrogen and oxygen atoms and is oriented parallel to 00 l plane; iii) layer stacking disorder increases as underlined by broadening of 001 reflection; iv) the diffraction pattern of Mt-CuPhen$_{semisat}$-NH_3 does not differ significantly from that of Mt-CuPhen$_{semisat}$.

UNCORRECTED

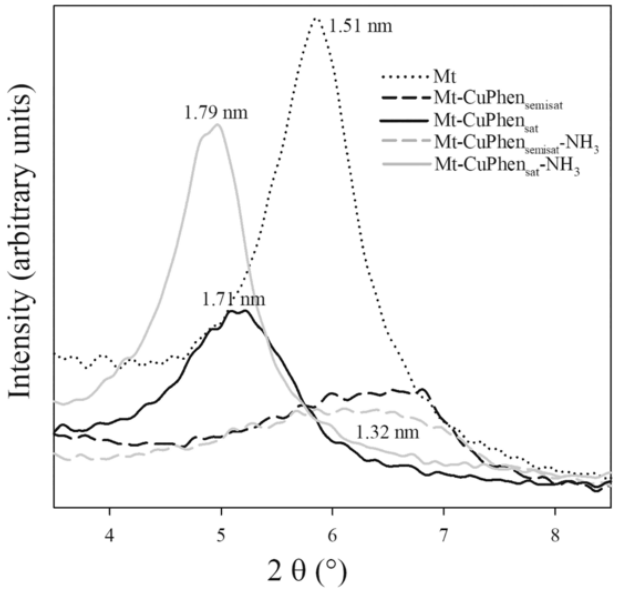

Fig. 6. X-ray diffraction patterns of Mt, Mt-CuPhen$_{sat}$ and Mt-CuPhen$_{semisat}$ before and after exposure to NH_3.

The treatment with 6 mM CuPhen solution shifts the 001 reflection position of Mt-CuPhen$_{sat}$ toward higher value (1.71 nm) with respect to Mt, consistently with the entry of CuPhen species coordinated by sulphate groups, approximately 0.71 nm thick (*i.e.*, the *c* unit cell value); ii) also in this case substitution mechanism affects interlayer features and intercalated molecules are likely oriented parallel to (00*l*) plane; iii) the interlayer space value of 0.71 nm suggests that Cu atoms present a distorted octahedral coordination, as evidenced in CuPhen crystal; iv) if compared to Mt-CuPhen$_{semisat}$, the 001 reflection intensity in Mt-CuPhen$_{sat}$ increases, suggesting an increase in the layer packing order. The exposure to NH_3 of Mt-CuPhen$_{sat}$ further increases layer distance (d_{001}-value = 1.79 nm) and reflection intensity, thus suggesting that NH_3 further enlarges the interlayer space and increases the order in the layer packing. Moreover, XRPD pattern of CuPhen$_{sat}$ before and after NH_3 exposure shows two additional reflections at 0.88 and 0.59 nm, corresponding to (002) and (003) lattice planes, respectively. These last reflections, absent in the original Mt sample, indicate that the intercalation of Mt with CuPhen in saturation condition causes a good ordering in the layer packing. The same increase of order and homogeneity in the interlayer was found for the intercalation of Mt by the μ-oxo dinuclear iron(III)-phenanthroline complex in saturation condition (Bernini et al., 2015).

For all samples the presence of the 060 reflection at 61.9 °2θ indicates that the dioctahedral nature of the original Mt sample is not affected by CuPhen treatments.

3.6. Thermal analysis

Thermogravimetric analyses (TGA) and their first derivative signal (DTGA) are given in Fig. 7a and b, respectively. The thermal behavior of natural Mt is characterized by three evident processes (Castellini et al., 2017). The first two mass loss signals with maxima at 83 °C (mass loss, wt = 10.57%) and at 154 °C (wt = 1.68%) are related to the loss of outer and inner sphere water molecules of the interlayer cation, respectively. The mass loss at 699 °C (wt = 2.64%) is due to the dehydroxylation of octahedral OH groups (Castellini et al., 2017). The overall mass loss at 1000 °C is wt = 16%. The three reactions descrived above only involve the release of H_2O (m/z = 18), as deduced by mass spectrometry of evolved gases.

Mass analyses of the evolved gases as a function of temperature for Mt-CuPhen$_{sat}$ and Mt-CuPhen$_{semisat}$ before and after exposure to NH_3 recorded at the m/z ratios 18 for H_2O, 15 for NH_3, 44 for CO_2, 30 for NO and NO_2, and 64 for SO_2 are reported in S4 (Fig. S4).

In the thermal range 25–1000 °C, the TGA and DTGA tracings (Fig. 7) of Mt-CuPhen$_{sat}$ and Mt-CuPhen$_{semisat}$ show: i) a well-defined reaction at 74 °C, associated to a mass loss of 3.62 wt% for Mt-CuPhen$_{sat}$ and 6.88 wt% for Mt-CuPhen$_{semisat}$, which involves the release of H_2O (m/z = 18). Note that, mostly for Mt-CuPhen$_{sat}$, the H_2O amount released during this reaction is found considerably lower than in Mt and that the reaction at 154 °C, due to inner-sphere H_2O molecules removal, is no longer present; as this last corresponds to the loss of coordination water of calcium, it indicates that a cation exchange was produced during the intercalation of CuPhen cations and no Ca^{2+} cations remain in the interlayer space; ii) a band at 327 °C mostly evident in Mt-CuPhen$_{sat}$ TGA curve (1.51 wt%), related to the loss of NO_2 (m/

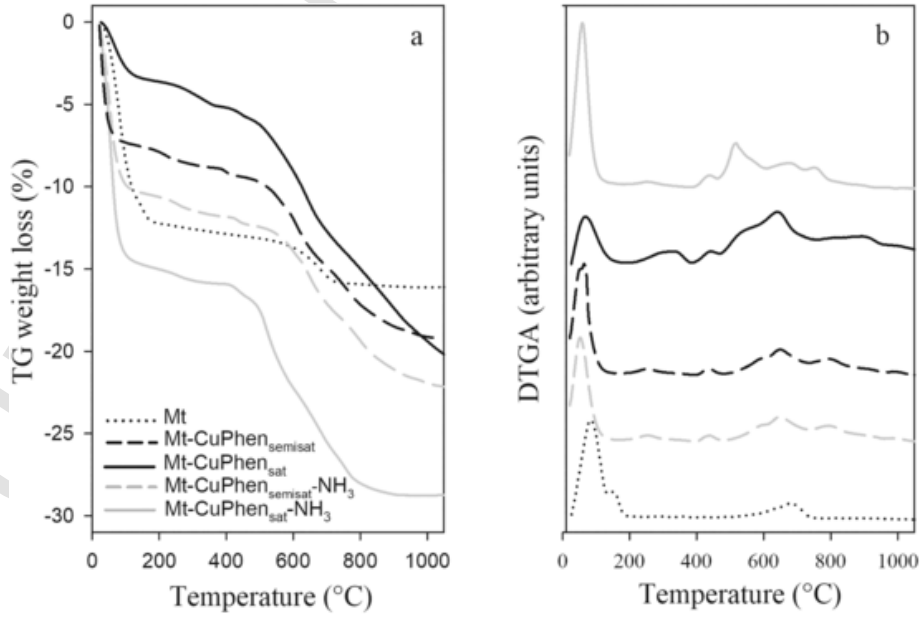

Fig. 7. Thermal analyses of Mt, Mt-CuPhen$_{sat}$ and Mt-CuPhen$_{semisat}$ before and after exposure to NH_3. DTGA curves are shifted on y axis for sake of clarity.

UNCORRECTED PROOF

z = 30), CO_2 (m/z = 44) and SO_2 (m/z = 64, this last only in Mt-CuPhen$_{sat}$) which can be attributed to the partial thermal decomposition of the CuPhen complex; iii) a composite band with three maxima at 442 (peak), 545 (shoulder) and 635 °C (peak) (total wt = 12.22% in CuPhen$_{sat}$ and total wt = 7.23% in Mt-CuPhen$_{semisat}$) due to the release of H_2O, CO_2, NO_2 and SO_2 (this last only in Mt-CuPhen$_{sat}$) associated to the decomposition of the Phen ligand in the CuPhen complex and to dehydroxylation of Al-OH and Mg-OH octahedral groups; iv) at $T > 700$ °C small peaks and shoulders suggest the complete thermal decomposition of the CuPhen complex. The total mass losses at 1000 °C are 20.9% and 19.2 wt% for Mt-CuPhen$_{sat}$ and Mt-CuPhen$_{semisat}$, respectively.

After exposure to NH_3 the overall mass loss strongly increases for both Mt-CuPhen$_{sat}$ (28.74 wt%) and CuPhen$_{semisat}$ (22.1 wt%); the greater change in mass loss compared to unexposed samples is mostly related to the release of the adsorbed NH_3 and water. In the temperature range 200–1000 °C, both DTGA curves are very similar to that of unexposed samples, with the only few exceptions: in Mt-CuPhen$_{sat}$-NH_3 the mass loss related to the band at 327 °C decreases (0.85% wt%) with respect to Mt-CuPhen$_{sat}$ and the shoulder at 545 °C shifts toward a lower temperature value and becomes more defined.

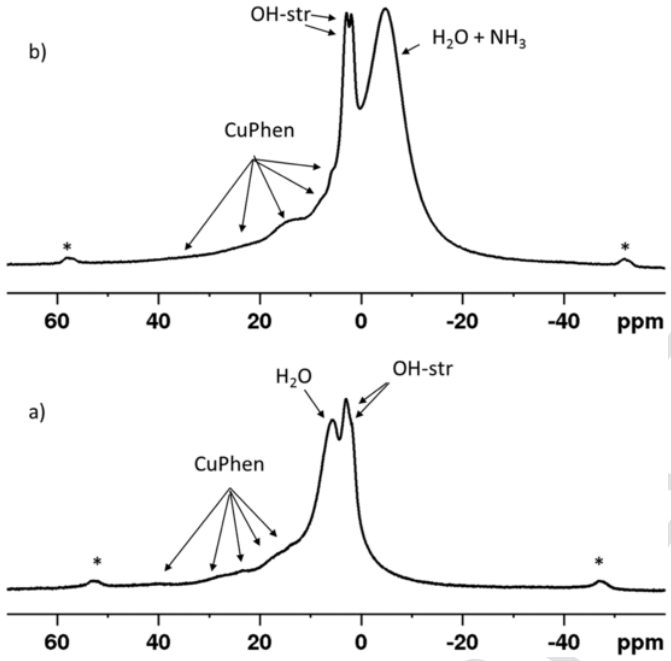

Fig. 8. ^{1}H MAS NMR spectra of a) Mt-CuPhen$_{sat}$ and b) Mt-CuPhen$_{sat}$-NH_3. (OH-str = structural hydroxyl).

3.7. NMR spectroscopy of Mt-CuPhen$_{sat}$ and Mt-CuPhen$_{sat}$-NH_3

The ^{1}H MAS NMR spectra of Mt-CuPhen$_{sat}$ and of Mt-CuPhen$_{sat}$-NH_3 are reported in Fig. 8. The spectrum of Mt-CuPhen$_{sat}$ (Fig. 8a) resembles those obtained for Mt-Fe^{3+}Phen (Sainz-Díaz et al., 2018). A series of peaks ranging from 42 to about 12 ppm, attributable to the ligand hydrogens, whereas two slightly resolved resonances at 3.0 and 1.8 ppm, attributable to structural OH (OH-str), are distinguished. A peak due to water protons is found at 5.8 ppm. When NH_3 is entrapped (Fig. 8b), phenanthroline signals are somewhat shielded and move to the 38–6 ppm range, suggesting a structural rearrangement of the complex. Furthermore, a broad signal, shielded with respect to those of structural OH at 3.2 and 1.9 ppm, appears at −4.7 ppm. This last signal can be attributed to exchanging hydrogens of Cu-coordinated water and ammonia molecules and its position should be intermediate between the chemical shifts of Cu-coordinated water and Cu-coordinated ammonia. In fact, a shielding, as a result of complexation, has been reported for hydrogens of coordinated ammonia in $Cu(NH_3)_6^{2+}$ (Wayland and Rice, 1966a), while a deshielding has been reported for water molecules in $Cu(H_2O)_6^{2+}$ (Wayland and Rice, 1966) the former being higher than the latter.

3.8. XAS spectroscopy

X- ray absorption experiments were performed to investigate the oxidation state of the copper absorbing atom, its coordination symmetry in the CuPhen crystals, and the effects originating from CuPhen intercalation in montmorillonite (Mt-CuPhen$_{sat}$ material). Besides, features in the absorption signal of the Mt-CuPhen$_{sat}$ material when exposed to NH_3 vapor were addressed.

Fig. 9a reports the XANES scans recorded at the Cu *K*-edge of CuPhen crystals and Mt-CuPhen$_{sat}$ material compared to the Cu foil and several other reference compounds previously detailed in the experimental section. The Cu *K*-absorption edge of XANES scans corresponds to the dipole-allowed 1 s → 4p transition. The Cu 4p orbitals split into $4p_{xy}$ and $4p_z$ due to ligand field splitting (Kim and Lee, 2003; Gaur and Shrivastava, 2012). Besides, a whiteline at the end of the edge related to 1 s → continuum transitions can be distinguished (Gaur et

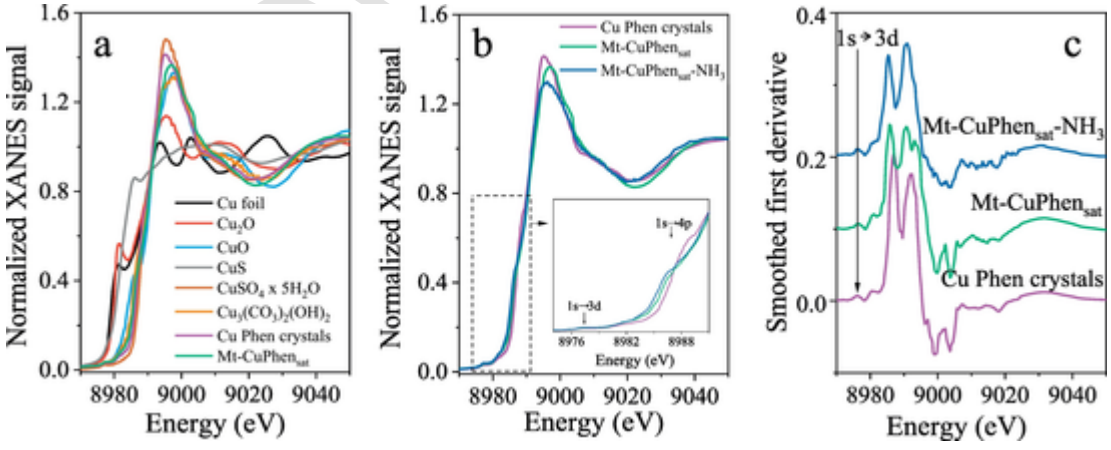

Fig. 9. (a) XANES spectra of CuPhen crystals and Mt-CuPhen$_{sat}$ compared with the spectrum of Cu foil and several reference compounds: Cu_2O, CuO, CuS, $CuSO_4x5H_2O$, and $Cu_3(CO_3)_2(OH)_2$. (b) XANES spectra of Mt-CuPhen$_{sat}$-NH_3 compared with Mt-CuPhen$_{sat}$ and CuPhen crystals. The inset displays a zoom of the peaks related to the 1 s → 3d and 1 s → 4p transitions. (c) Smoothed first derivative of absorption signal of CuPhen crystals, Mt-CuPhen$_{sat}$ and Mt-CuPhen$_{sat}$-NH_3. The 1 s → 3d transition, characteristic of Cu^{2+} compounds, is remarked on Fig. 9c.

al., 2016). For both CuPhen crystals and the Mt-CuPhen$_{sat}$ the energy value of absorption edge falls close to reference compounds with the Cu in divalent form.

The Cu^{2+} compounds are in a d^9 configuration and most of them present a pre-edge (around 8977 eV) associated with the dipole-forbidden/quadrupole allowed 1 s → 3d transition (Kim and Lee, 2003; Gaur and Shrivastava, 2012) indicating the existence of 3d holes. The presence of this weak absorption pre-edge, not clear in the XANES scans, is well evidenced by first derivative of signal (Fig. 9c), thus confirming the divalent state of copper for the CuPhen crystals and the Mt-CuPhen$_{sat}$ complex.

Despite the fact that the CuPhen crystals and Mt-CuPhen$_{sat}$ have the same oxidation state (2+), XANES signal presents differences in the position of the absorption edge, intensity of the pre-edge, intensity of the edge shoulder, whiteline intensity and shape of XANES spectra (Fig. 9). These variations can be explained by the different nature of ligand and the coordination geometry of the photo-absorber atom (Cu) (Palladino et al., 1993; Kim and Lee, 2003). For example, the reference CuO and $CuSO_4 \times 5H_2O$ are in same divalent form, but CuO has a square planar geometry, while the reference $CuSO_4 \times 5H_2O$ is in an octahedral geometry (Gaur et al., 2016), which induces those differences in the XANES response. For the case of CuPhen crystals, the XANES profile is quite close to that of reference $CuSO_4 \times 5H_2O$, but with a lower intensity of edge shoulder related to a decrease of the 4p density of states. The absorption edge displacement toward smaller energies and the decreasing intensity of whiteline approaching the XANES profile of the CuO reference is indicative of the distorted Cu octahedral coordination of CuPhen crystals, as revealed by single crystal X-ray diffraction and UV–Visible measurements (SI 1, Fig. SI1). For the Mt-CuPhen$_{sat}$ the XANES signal features are similar to the ones present in the references CuO and CuPhen crystals, nevertheless, closer to that of the CuPhen crystals, even if with a slight increase in the intensity of the pre-edge feature corresponding to the 1 s → 3d transition.

These line-shape differences, although small, for a same metallic atom are indicative of different coordination geometries (Gaur et al., 2016). Therefore, considering the DR UV–Vis and X-ray diffraction results, not only the distorted octahedral coordination of the Mt-CuPhen$_{sat}$, but also a larger distorted character than the crystals can be confirmed. The increase in the distortion may be due to the interaction with clay.

The comparison between the XANES spectra of CuPhen crystals, Mt-CuPhen$_{sat}$ and Mt-CuPhen$_{sat}$-NH_3 (Fig. 9b) clearly shows that the absorption signal in Mt-CuPhen$_{sat}$ does not change significantly after NH_3 exposure. Specifically, the position of the absorption edge falls close to that of compounds with the Cu in divalent form. The divalent Cu oxidation state, after NH_3 exposure of Mt-CuPhen$_{sat}$, is confirmed by the presence of weak pre-edge in the first derivative of the XANES signal (Fig. 9c).

However, some differences in the intensity of the absorption edge, intensity of the whiteline and shape of XANES profile can be observed. After the NH_3 exposure, a lower intensity of XANES whiteline, an increase of the intensity at the absorption pre-edge and an increase of the edge shoulder intensity (see inset in Fig. 9b) with respect to the structure of Mt-CuPhen$_{sat}$ can be noted. Comparison of XANES signal of Mt-CuPhen$_{sat}$ after NH_3 exposure, with the signal from $CuSO_4 \times 5H_2O$ reference reveals more similitudes to a compound with lower coordination, such as CuO, than to octahedral coordinated $CuSO_4 \times 5H_2O$ reference. All these features together with the DR UV–Vis measurements (Fig. 4) may correspond to a larger distortion, induced by the exposure to NH_3 gas, in the octahedral structure of CuPhen complex.

Combariza and Vachet (2004) suggested a modification of Cu coordination after NH_3 adsorption from planar four-fold to five-fold coordination with the addition of an out-of-plane Cu-NH_3 bonding. If in Mt-CuPhen$_{sat}$ Cu^{2+} coordination is pseudo-octahedral, the previously described mechanism is not feasible. X-ray diffraction and XANES (only available for Mt-CuPhen$_{sat}$ sample) data suggest, for both Mt-CuPhen$_{semisat}$ and Mt-CuPhen$_{sat}$, a topologically similar coordination for Cu^{2+} before and after NH_3 adsorption. The fact that the interlayer space keeps constant in Mt-CuPhen$_{semisat}$ after the adsorption of NH_3 suggests that, probably, NH_3 binds to CuPhen replacing the two water ligands, allowing Cu^{2+} to retain square planar coordination. In Mt-CuPhen$_{sat}$ the same replacement of H_2O molecules with NH_3 takes place allowing retention of the octahedral geometry by the complex (actually, a small increase of the d_{001}-value was observed and may be related the higher interlayer filling in the saturated sample). Therefore, previously discussed mechanism assuming modification of Cu coordination does not seem applicable for the studied samples.

4. Conclusions

The set of experimental data indicates that the Mt-CuPhen ensures high performance in removing NH_3 from gaseous phase. At room temperature, the process occurs even at extremely low NH_3 pressure (at least up to 5.7 Pa). The intercalation of CuPhen in Mt interlayer consists of two steps depending on complex concentration and involving Cu^{2+} in two different coordination arrangements. In the first step of adsorption (up to semi-saturation), Cu^{2+} likely assumes a square planar coordination. The second step (up to saturation) leads instead to a progressive change of Cu^{2+} coordination yielding to a distorted octahedral geometry. The different interlayer configuration strongly affects gaseous NH_3 adsorption. The uptake per Cu^{2+} ion is higher in the former step, when Mt interlayer is more hydrated and thus NH_3 adsorption is favored by a more hydrophilic environment. This fact confirms the prominent role of the structural properties of the adsorbent mineral in the gas-trapping process (Castellini et al., 2019b). Mt-CuPhen stably retains NH_3 and can be easily regenerated even at 110 °C. It is, therefore, a promising material for industrial and environmental applications.

Uncited reference

Acknowledgments

We acknowledge MIUR-PRIN2017 - PROGETTO N. 2017L83S77, the Spanish CRG BM25-SpLine, the Spanish Ministry of Science Innovation and Universities (MICIU), the Spanish National Research Council (CSIC) and The European Synchrotron (The ESRF) for the use of the synchrotron radiation facilities and financial support, the LADAC laboratory of DSCG, University of Modena and Reggio Emilia. A.S. acknowledges the financial support from the Comunidad de Madrid for an "Atracción de Talento Investigador" contract (No. 2017-t2/IND5395).

Declaration of Competing Interest

none

Appendix A. Supplementary data

Supplementary data to this article can be found online at https://doi.org/10.1016/j.clay.2019.105386.

References

Barin, G., Peterson, G.W., Crocella, V., Xu, J., Colwell, K.A., Nandy, A., Reimer, J.A., Bordiga, S., Long, J.R., 2017. Highly effective ammonia removal in a series of Bronsted acidic porous polymers: investigation of chemical and structural variations. Chem. Sci. 8, 4399–4409.

Bergaya, F., Lagaly, G., 2011. Intercalation processes of layered minerals. In: Brigatti, M.F., Mottana, A. (Eds.), Layered Mineral Structures and their Application in Advanced Technologies, EMU, Notes in Mineralogy, Volume 11. European Mineralogical Union and the Mineralogical Society of Great Britain, London, pp. 259–284. (Chapter 7).

UNCORRECTED PROOF

Bernini, F., Castellini, E., Malferrari, D., Borsari, M., Brigatti, M.F., 2015. Stepwise structuring of the adsorbed layer modulates the physico-chemical properties of hybrid materials from phyllosilicates interacting with the μ-oxo Fe^{+3} phenanthroline complex. Microporous Mesoporous Mater. 211, 19–29.

Bernini, F., Castellini, E., Malferrari, D., Castro, G.R., Sainz-Díaz, C.I., Brigatti, M.F., Borsari, M., 2017. Effective and selective trapping of volatile organic sulfur derivatives by montmorillonite intercalated with a μ-oxo Fe(III)−Phenanthroline complex. Appl. Mater. Interfaces 9, 1045–1056.

Brigatti, M.F., Malferrari, D., Laurora, A., Elmi, C., 2011. Structure and mineralogy of layer silicates: Recent perspectives and new trends. In: Brigatti, M.F., Mottana, A. (Eds.), Layered Mineral Structures and their Application in Advanced Technologies, EMU, Notes in Mineralogy. European Mineralogical Union and the Mineralogical Society of Great Britain, London, pp. 1–71.

Brigatti, M.F., Sainz Díaz, C.I., Borsari, M., Bernini, F., Castellini, E., Malferrari, D., 2017. Crystal chemical characterization and computational modelling of a μ-oxo Fe(III) complex with 1,10-phenanthroline clarify its interaction and reactivity with montmorillonite. Rend. Fis. Acc. Lincei 28, 605–614.

Busca, G., Pistarino, C., 2003. Abatement of ammonia and amines from waste gases: a summary. J. Loss Prevent Proc. 16, 157–163.

Castellini, E., Bernini, F., Borsari, M., Brigatti, M.F., Castro, G.R., Malferrari, D., Medici, L., Mucci, A., 2017. Baseline studies of the Clay Minerals Society Source Clay montmorillonite STx-1b. Clay Clay Miner. 65, 220–233.

Castellini, E., Malferrari, D., Bernini, F., Mucci, A., Borsari, M., Brigatti, M.F., 2019. Structural properties of adsorbent phyllosilicates rule the entrapping ability of intercalated iron-phenanthroline complex towards thiols. Microporous Mesoporous Mater. 285, 150–160.

Castellini, E., Malferrari, D., Bernini, F., Sainz-Díaz, C.I., Mucci, A., Sola, M., Brigatti, M.F., Borsari, M., 2019. Trapping at the solid-gas interface: selective adsorption of naphthalene by montmorillonite intercalated with a Fe(III)-phenanthroline complex. ACS Omega 4, 7785–7794.

Chen, Y., Li, L., Li, J., Ouyang, K., Yang, J., 2016. Ammonia capture and flexible transformation of M-2(INA) (M = Cu, Co, Ni, Cd) series materials. J. Hazard. Mater. 306, 340–347.

Chung, Y.C., Huang, C., Liu, C.H., Bai, H., 2001. Biotreatment of hydrogen sulfide- and ammonia-containing waste gases by fluidized bed bioreactor. J. Air Waste Manag. Assoc. 51, 163–172.

Combariza, M.Y., Vachet, R.W., 2004. Effect of coordination geometry on the gas-phase reactivity of four-coordinate divalent metal ion complexes. J. Phys. Chem. A 14, 1757–1763.

Gaur, A., Shrivastava, B.D., 2012. A comparative study of the methods of speciation using X-ray absorption fine structure. Acta Phys. Pol. A 121, 647–652.

Gaur, A., Klysubun, W., Nitin Nair, N., Shrivastava, B.D., Prasad, J., Srivastava, K., 2016. XAFS study of cooper(II) com plexes with square planar and square pyramidal coordination geometries. J. Mol. Struct. 1118, 212–219.

Giustetto, R., Seenivasan, K., Bonino, F., Ricchiardi, G., Bordiga, S., Chierotti, M.R., Gobetto, R., 2011. Host/guest interactions in a sepiolite-based Maya Blue pigment: a spectroscopic study. J. Phys. Chem. C 115, 16764–16776.

Gregg, S.J., Sing, K.S.W. (Eds.), 1982. Adsorption Surface Area and Porosity. Academic Press, London.

He, S., Zhang, C., Yang, M., Zhang, Y., Xu, W., Cao, N., He, H., 2007. Selective catalytic oxidation of ammonia from MAP decomposition. Sep. Purif. Technol. 58, 73–178.

Hu, X., Guo, J., Liu, C., Zen, H., Wang, Y., Du, W., 2009. Two new supermolecular structures of organic–inorganic hybrid compounds: $[Zn(phen)(SO_4)(H_2O)_2]n$ and $[Cu(phen)(H_2O)_2]SO_4$ (phen = 1,10-phenanthroline). Inorganica Chim. Acta 362, 3421–3426.

Jabłonska, M., Palkovits, R., 2016. Copper based catalysts for the selective ammonia oxidation into nitrogen and water vapour-recent trends and open challenges. Appl. Catal. B-Environ. 181, 332–351.

Kim, W.B.K., Lee, J.S., 2003. Quantitative XANES analysis of cuprous dibromide complex formed in the oxidative carbonynation of phenols. J. Phys. Chem. B 107, 9195–9202.

Lenihan, S., Curtin, T., 2009. The selective oxidation of ammonia using copper-based catalysts: the effects of water. Catal. Today 145, 85–89.

Liu, E., Sarkar, B., Wang, L., Naidu, R., 2016. Copper-complexed clay/poly-acrylic acid composites: extremely efficient adsorbents of ammonia gas. Appl. Clay Sci. 121–122, 154–161.

Malferrari, D., Castellini, E., Bernini, F., Serrano Rubio, A., Castro, G.R., Sainz-Díaz, C.I., Caleffi, M., Brigatti, M.F., Borsari, M., 2018. Chemical trapping of gaseous H_2S at high and low partial pressures by an iron complex immobilized inside the montmorillonite interlayer. Microporous Mesoporous Mater. 265, 8–17.

Mayera, R.W., Häveckerb, M., Knop-Gerickeb, A., Schlöglb, R., 2011. Investigation of ammonia oxidation over copper with in situ NEXAFS in the soft X-ray range: influence of pressure on the catalyst performance. Catal. Lett. 74, 115–119.

Palladino, L., Della Longa, S., Reale, A., Belli, M., Scafati, A., Onori, G., Santucci, A., 1993. X-ray absorption near edge structure (XANES) of Cu(II)–ATP and related compounds in solution: quantitative determination of the distortion of the Cu site. J. Chem. Phys. 98, 2720.

Ravel, B., Newville, M., 2005. ATHENA, ARTEMIS, HEPHAESTUS: Data analysis for X-ray absorption spectroscopy using IFEFFIT. J. Synchrotron Radiat. 12 (4), 537–541.

Sainz-Díaz, C.I., Bernini, F., Castellini, E., Malferrari, D., Borsari, M., Mucci, A., Brigatti, M.F., 2018. Experimental and Theoretical Investigation of Intercalation and Molecular Structure of Organo-Iron Complexes in Montmorillonite. Phys. Chem. C 122, 25422–25432.

Sing, K.S.W., Everett, D.H., Haul, R.A.W., Moscou, L., Pierotti, R.A., Wayland, B.B., Rice, W.L., 1966. Proton contact shifts for the hexaammine complexes of Cu(II) and Ni(II) perchlorate: comments on knight shifts for solutions of sodium in ammonia. J. Chem. Phys. 45, 3150.

Wayland, B.B., Rice, W.L., 1966. Contact shift studies of some paramagnetic hexaaquo metal ion complexes. Inorg. Chem. 5, 54–57.

Wójtowicz, M.A., Miknis, F.P., Grimes, R.W., Smith, W.W., Serio, M.A., 2000. Control of nitric oxide, nitrous oxide, and ammonia emissions using microwave plasmas. J. Hazard. Mater. 74, 81–89.

Yue, W., Zhang, R., Liu, N., Chen, B., 2014. Selective catalytic oxidation of ammonia to nitrogen over orderly mesoporous $CuFe_2O_4$ with high specific surface area. Chin. Sci. Bull. 59, 3980–3986.

UNCORRECTED PROOF